Materials Advances

ROYAL SOCIETY OF CHEMISTRY

PAPER

View Article Online
View Journal | View Issue

Cite this: *Mater. Adv.*, 2022, 3, 6831

A nano-structured nickel trithiocarbonate complex supported on g-C_3N_4 as an efficient electrocatalyst for urea electro-oxidation†

Debojit Ghosh,[a] Rumeli Banerjee,[a] Gopala R. Bhadu,[b] Samanka Narayan Bhaduri,[a] Anup Mondal,[a] Divesh N. Srivastava[b] and Papu Biswas *[a]

Received 17th March 2022,
Accepted 15th July 2022

DOI: 10.1039/d2ma00308b

rsc.li/materials-advances

Electrolysis of water is emerging as a potential technique for producing green hydrogen. However, the large overpotential due to the sluggish kinetics involved with the oxygen evolution reaction (OER) is coercing scientific communities toward finding alternative ways of hydrogen generation. Recently, the urea oxidation reaction (UOR) has evolved as a promising anode reaction for the electrocatalytic production of hydrogen. Herein, we report the fabrication of a composite of a nanostructured nickel(II) trithiocarbonate (Ni-ttc-d) complex with g-C_3N_4 fabricated by a simple mechanochemical method and demonstrate its use as a robust and efficient catalyst for the UOR. The 35-Ni-ttc-d/g-C_3N_4 composite with 35 weight% of Ni-ttc-d displayed the highest electrochemical surface area (ECSA) and double-layer capacitance (C_{dl}) along with the lowest R_{ct} and required a potential of 1.38 V (*vs.* RHE) to achieve a current density of 10 mA cm^{-2} for the UOR, which is about 290 mV lower than that of the OER process. The Ni-ttc-d/C_3N_4 composite also showed excellent amperometric and potentiometric stability.

Introduction

The emergent concern about the global energy crisis due to the depletion of fossil fuels has escalated the urge to explore clean and renewable alternative energy resources.[1–3] Hydrogen, as a fuel, is the best alternative energy resource due to its unparalleled environmentalfriendliness and high caloric features for sustainable development. The electrochemical generation of hydrogen is considered the most eco-friendly pathway. Thus, water splitting has drawn attention as a promising route to produce hydrogen without causing environmental damage. Electrocatalytic water splitting comprises a hydrogen evolution reaction (HER) at the cathode and an oxygen evolution reaction (OER) at the anode.[2,4] Notably, the high over-potential of the OER arising from its slow four-proton-coupled reaction kinetics makes the entire process of water splitting less efficient. Thus, replacements for the OER with more readily oxidizable molecules, such as urea, hydrazine, methanol, ammonia, glycerol, *etc.*, are a suitable alternative to make the energy conversion more competent.[5–12]

Urea, a bio waste, often gives rise to severe health and environmental complications. It produces ammonium sulfate and nitrate in the atmosphere and is commonly present as a waste product in industrial and sanitary wastewater, causing water pollution.[13–15] However, urea is an attractive alternative in electrochemical hydrogen production owing to its 6.67 wt% hydrogen content, fairly good energy density (16.9 MJ L^{-1}), stability, ease of storage, and easy availability in wastewater.[14–18] Thus, the use of urea from wastewater in electrochemical hydrogen generation simultaneously focuses on solving the energy crisis and remediation of wastewater.[14–20]

Moreover, the UOR requires a theoretical potential of 0.37 V (*vs.* SHE), which is considerably less than that of water electrolysis (1.23 V) and ideally produces hydrogen at lower energy than water electrolysis.[3,21] Urea electrolysis for hydrogen generation involves the following reactions:

$$\text{Anode: } CO(NH_2)_2 + 6OH^- \rightarrow N_2 + CO_2 + 5H_2O + 6e^- \quad (E^0 = -0.46 \text{ V } vs. \text{ SHE}) \quad (1)$$

$$\text{Cathode: } 6H_2O + 6e^- \rightarrow 3H_2 + 6OH^- \quad (E^0 = -0.83 \text{ V } vs. \text{ SHE}) \quad (2)$$

$$\text{Overall reaction: } CO(NH_2)_2 + H_2O \rightarrow N_2 + 3H_2 + CO_2 \quad (E^0 = 0.37 \text{ V}) \quad (3)$$

[a] *Department of Chemistry, Indian Institute of Engineering Science and Technology, Shibpur, Howrah 711 103, West Bengal, India. E-mail: papubiswas_besus@yahoo.com*
[b] *Department of Analytical Science, Central Salt & Marine Chemicals Research Institute, Gijubhai, Badheka Marg, Bhavnagar, 364002 Gujarat, India*

† Electronic supplementary information (ESI) available: Fig. S1–S11 and Tables S1–S5. See DOI: https://doi.org/10.1039/d2ma00308b

However, the UOR also has characteristically slow kinetics arising from its slow six-electron transfer process. Accordingly, it is essential to develop active electrocatalysts for widespread application. Oxidation of urea in neutral solutions over noble metal surfaces (Ti–Pt, Ti–Pt–Ir, *etc.*) has been meticulously studied.[22,23] However, the high cost, scarcity, and the limited catalytic activity of the noble metal-based catalysts deter their real-world application on a large scale.[24] Botte and co-workers first reported the UOR using low-cost Ni-based catalysts in an alkaline medium.[25] To date, numerous Ni-based catalysts (such as Rh–Ni, Ru–Ni, Pt–Ni, Pt–Ir–Ni, nano-structured nickel oxides, nickel hydroxides, Ni–Co bimetallic hydroxide, Ni-WC/C, $NiCo_2O_4$, $LaNiO_3$, NiF_2/Ni_2P hybrid, Ni–Co–WC/C, nickel nitride, Mn–Ni_3S_2, nickel borate, Ni-MOF)[14,21,26–45] have been reported as highly active catalysts for high-performance UOR. Botte and co-workers proposed the formation of NiOOH as an intermediate state, which acts as an active site for urea electro-oxidation on a nickel surface.[46–48] However, generation of NiOOH often leads to a sluggish reaction rate, higher over-potential, low stability, and eventually deactivation of nickel catalysts.[48,49] Hence, the synthesis of stable, efficient, inexpensive nickel-based catalysts is of significant interest.

In this work, we report the synthesis of a nano-structured simple nickel(II) trithiocarbonate (Ni-ttc) complex supported on active g-C_3N_4, having excellent UOR activity and low over-potential for the current density of 10 mA cm^{-2}. Recent reports reveal that the immobilization of Ni-based catalysts on carbon surfaces can augment the efficiency of the UOR due to the synergetic effect.[14,35,50–54] Graphitic carbon nitride (g-C_3N_4) has emerged as a potential non-toxic photocatalyst due to its easy synthesis method and low cost,[55–57] which is widely used for organic transformation, photo-electrochemical water splitting, *etc.*[58–63] The heptazine units and other amine groups in g-C_3N_4 offer excellent coordination sites for Ni(II).[53] Thus, the g-C_3N_4 architecture empowers electron/ion transport, exposes more accessible electroactive sites for reactions, and provides outstanding mechanical stability during the long-term electrolysis process. Also, the high conductivity and flexible characteristics of g-C_3N_4 are not only appropriate for immobilizing active materials on the surface but also simplify electrolyte immersion and swift dissipation of gaseous products. The present Ni-ttc-d/g-C_3N_4 catalyst is very easy to fabricate, and the work highlights the possibilities of energy-saving and high-efficiency hydrogen generation in the future.

Experimental section

Materials

Nickel nitrate hexahydrate, carbon disulfide, cyclohexane thiol, and KOH were purchased from Spectrochem Pvt. Ltd. Melamine and urea were obtained from Sigma-Aldrich. All other chemicals and solvents were purchased from locally available commercial sources and used without further purification. g-C_3N_4 was synthesized following the method reported previously.[64] All the solutions were prepared using purified and de-ionized water (Milli-Q grade, Millipore).

Synthesis of potassium cyclohexyl trithiocarbonate (ttc)

Cyclohexane thiol (0.581 g, 5 mmol) was taken in a 250 mL round bottom flask and finely crushed KOH (0.28 g, 5 mmol) powder was quickly added to it. The resulting mixture was stirred vigorously for 30 min. Carbon disulfide (0.42 g, 5.5 equivalents) in diethyl ether (50 mL) was then added to the solution and stirred for a further 4 h, during which a golden yellow precipitate started to appear. The precipitate was filtered, washed with ether, and recrystallized.

Synthesis of the nickel cyclohexyl trithiocarbonate complex (Ni-ttc)

Potassium cyclohexyl trithiocarbonate (0.46 g, 2 mmol) was dissolved in ethanol (25 mL) and $Ni(NO_3)_2{\cdot}6H_2O$ (0.29 g, 1 mmol) solution in 10 mL ethanol was added to it. The resulting solution was stirred for 30 min to yield a brown precipitate. The product was filtered and washed thrice with ethanol.

Preparation of nano-structured nickel cyclohexyl trithiocarbonate (Ni-ttc-d)

Brown Ni-ttc (0.44 g, 1 mmol) was taken in 5 mL of dimethyl formamide (DMF) in a Schlenk tube, and the mixture was heated at 180 °C. The heating was continued for 8 h, and finally, fine blackish brown Ni-ttc-d was collected by centrifugation.

Preparation of Ni-ttc-d/g-C_3N_4 composites

The as-prepared Ni-ttc-d (35 mg) was mixed in an agate mortar with g-C_3N_4 (65 mg) and homogenized by grinding for at least 1 h to obtain Ni-ttc-d/g-C_3N_4 composites. The Ni-ttc-d/g-C_3N_4 composites were prepared in different weight proportions of Ni-ttc-d and g-C_3N_4, such as 50%:50%, 35%:65%, 15%:85%, and 5%:95%. The samples were named X-Ni-ttc-d/g-C_3N_4, where X is the weight percentage of Ni-ttc-d.

Preparation of catalyst ink and the working electrode

2 mg of catalyst (X-Ni-ttc-d/g-C_3N_4) was added to a mixture of 30 μL of 10 wt% Nafion solution and 570 μL of de-ionized water. The mixture was subsequently sonicated for 60 mins to prepare the catalyst ink. The glassy carbon (GC) electrode was cleaned thoroughly with a 0.05 micron alumina powder slurry followed by rinsing in distilled water, isopropanol, and acetone and then dried in air. The catalyst ink was drop cast on the cleaned GC electrode to maintain an average loading of $\sim$0.4 mg cm^{-2} and used as the working electrode.

Electrochemical studies

The electrochemical performances of the modified working electrode were studied by cyclic voltammetry (CV) and linear sweep voltammetry (LSV) at room temperature using a CH Instrument CHI660E Electrochemical Workstation. A conventional three-electrode set up, comprising the modified GC working electrode, a saturated calomel electrode (SCE) as a reference electrode, and a Pt wire as the counter electrode was utilized for the electrochemical measurements.

The electrocatalytic urea oxidation was performed using Ni-ttc-d/g-C_3N_4, Ni-ttc-d, Ni-ttc, and g-C_3N_4 catalysts in an alkaline medium at a scan rate of 50 mV s^{-1}. The data were converted to a RHE (reversible hydrogen electrode) using eqn (4):

$$E_{RHE} = E_{SCE} + 0.059pH + 0.242 \quad (4)$$

where E_{RHE} is the potential against the RHE, E_{SCE} is the potential recorded using the SCE as a reference electrode, and the value 0.242 is the standard redox potential for the SCE *vs.* RHE. The urea electro-oxidation of the catalysts was performed in 1 M KOH with 0.33 M urea. Electrochemical impedance spectra (EIS) were recorded in the frequency range from 100 kHz to 0.01 kHz. Chronopotentiometry and chronoamperometry measurements were used to assess the long-term stability of the electrocatalysts.

Material characterizations

The powder XRD analyses of the catalysts were performed using a Philips PW 1140 parallel beam X-ray diffractometer with monochromatic Cu Kα radiation (λ = 1.540598 Å) operated at 40 kV and 40 mA with a step size of 0.008 and a scanning rate of 0.02 s^{-1} in the 2θ range of 10–80°. The elemental composition of the catalysts was analyzed by XPS measurements using a PHI 5000 Versa Probe III instrument. The morphology and microstructure of the materials were characterized *via* field emission scanning electron microscopy (FESEM, JEOL JSM-7610F) using an accelerating voltage of 15 kV. FE-SEM-EDS analysis and particle mapping were performed in the same SEM instrument equipped with an Oxford Instruments X-Max^N X-ray detector. Transmission electron microscopy (TEM), high-resolution TEM (HRTEM), TEM-EDS analysis, and particle mapping were performed using a JEOL-2100F transmission electron microscope with an acceleration voltage of 200 kV. The N_2 adsorption–desorption isotherms were measured using a NOVA 2200e surface area and pore size analyzer. The specific surface areas were calculated using the NLDFT method. The samples were degassed under a nitrogen flow at 373 K for 6 h to remove impurities adsorbed on the catalyst's surface before the sorption experiment. TGA-DTA analysis was performed using a PerkinElmer TGA 4000 instrument. The FT-IR spectra were recorded on an Agilent Cary 630 spectrometer using the Diamond ATR facility attached with it. Diffused reflectance spectra were obtained using an Agilent Cary 5000 UV-vis-NIR spectrometer. ^{1}H NMR spectra were recorded on a Bruker Avance IV 400 MHz NMR spectrometer. NMR spectra were recorded at room temperature with $CDCl_3$. ICP-OES analysis was done with a PerkinElmer Optima 2000 instrument. The sample was digested in HCl for 30 min, evaporated to dryness and redissolved in water before analysis.

Results and discussion

The preparation of Ni-ttc, Ni-ttc-d, and Ni-ttc-d/g-C_3N_4 is illustrated in Scheme 1. The Ni-ttc-d/g-C_3N_4 composites were prepared by grinding Ni-ttc-d and g-C_3N_4 in the requisite quantity in a mortar with a pestle. This mechanochemical method is a rapid, solvent-free facile way to fabricate nanocomposites.[54,65,66]

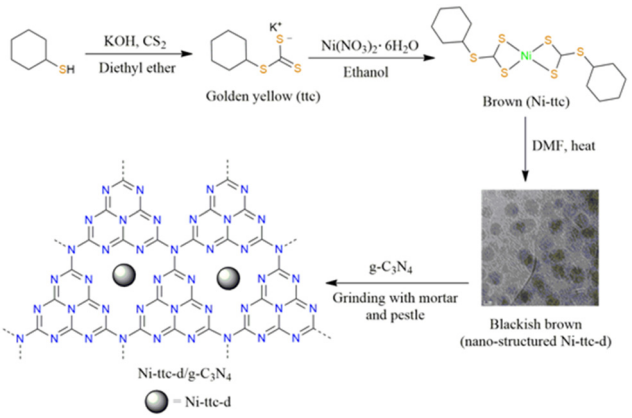

Scheme 1 Preparation of Ni-ttc, Ni-ttc-d, and Ni-ttc-d/g-C_3N_4.

The X-ray diffraction patterns (XRD) of Ni-ttc and Ni-ttc-d are shown in Fig. 1a and b. Ni-ttc displayed six well-defined diffraction peaks at 28.3, 40.5, 50.2, 58.7, 66.4, 67.4, and 73.7°. The same diffraction peaks appeared for Ni-ttc-d, which confirms that no significant change in the crystal structure occurred during the heat treatment in DMF. The XRD patterns of g-C_3N_4 and 35-Ni-ttc-d/g-C_3N_4 (Fig. 1c and d) display two distinct diffraction peaks, a weak peak at 13.0° and a strong one at 27.4° corresponding to the (100) and (002) planes, respectively, of the hexagonal lattice. The weak peak appears due to the in-plane structural packing motif of tris-triazine units, which corresponds to a hole-to-hole distance d = 0.681 nm in the nitride pores.[67] The strong peak is attributed to the interlayer stacking of aromatic segments with a distance of 0.326 nm.[67] A small peak at about 30° appeared in 35-Ni-ttc-d/g-C_3N_4, which is due to the presence of Ni-ttc-d.

Fig. S1 (ESI†) shows the FT-IR spectra of g-C_3N_4 and 35-Ni-ttc-d/g-C_3N_4. The broad peak around 3100 cm^{-1} is observed due to the stretching vibration of the N–H bond. The five medium intensity peaks observed within the range 1650–1200 cm^{-1} are attributed to the aromatic C–N stretching vibrations. The sharp peak at around 800 cm^{-1} corresponds to the *s*-triazine ring organization in g-C_3N_4. The similar features of the FT-IR spectra of g-C_3N_4 and 35-Ni-ttc-d/g-C_3N_4 indicate that the loading of Ni-ttc-d does not affect the basic structures of g-C_3N_4. The FT-IR spectra of trithiocarbonate ligands, Ni-ttc and Ni-ttc-d are shown in Fig. S2 (ESI†). The absorption behaviour of the samples was studied by UV-vis-NIR diffuse reflectance spectra (Fig. S3, ESI†). Ni-ttc and Ni-ttc-d exhibited a broad peak in the visible and NIR region, as expected for Ni(II) complexes. The absorption edge of g-C_3N_4 is estimated around 450 nm. After loading Ni-ttc-d on g-C_3N_4, the composite material exhibits absorption peaks in a higher wavelength region. The N_2 adsorption-desorption isotherms of the synthesized catalysts g-C_3N_4 and 35-Ni-ttc-d/g-C_3N_4 were measured to illustrate the specific surface area (Fig. S4, ESI†). The results are presented in Table S1 (ESI†). It is evident from the isotherms that both g-C_3N_4 and 35-Ni-ttc-d/g-C_3N_4 have type IV isotherms with type

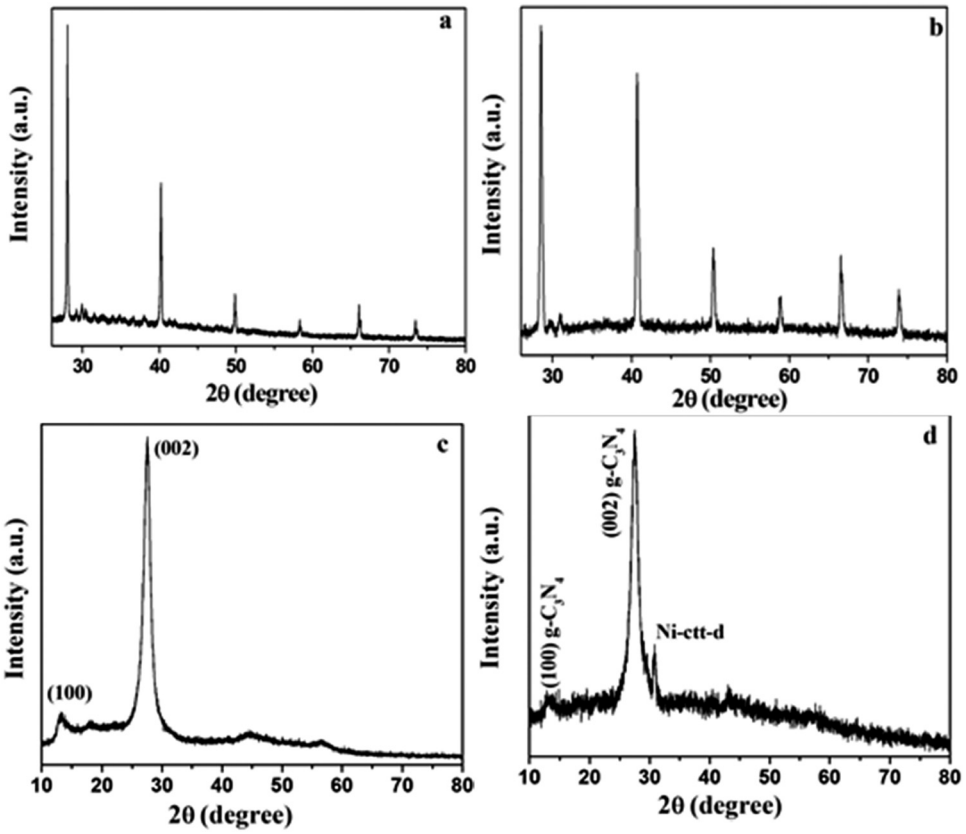

Fig. 1 Powder XRD patterns of (a) Ni-ttc, (b) Ni-ttc-d, (c) g-C_3N_4, and (d) 35-Ni-ttc-d/g-C_3N_4.

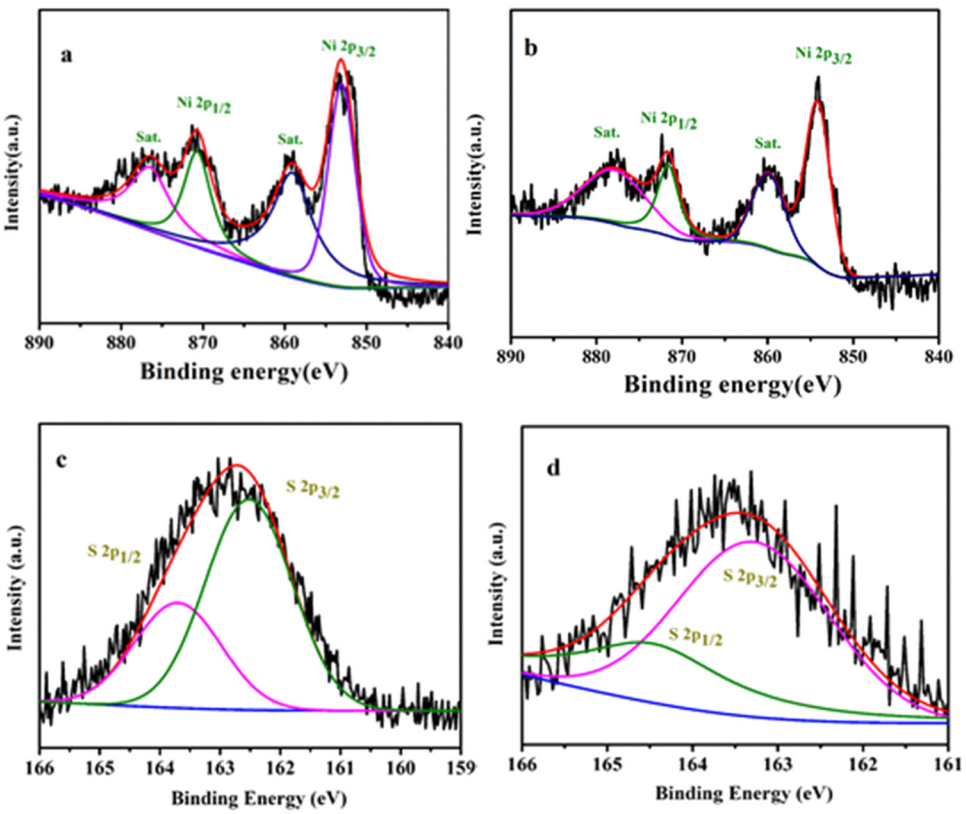

Fig. 2 High resolution XPS spectra of (a and b) Ni 2p and (c and d) S 2p in Ni-ttc and Ni-ttc-d.

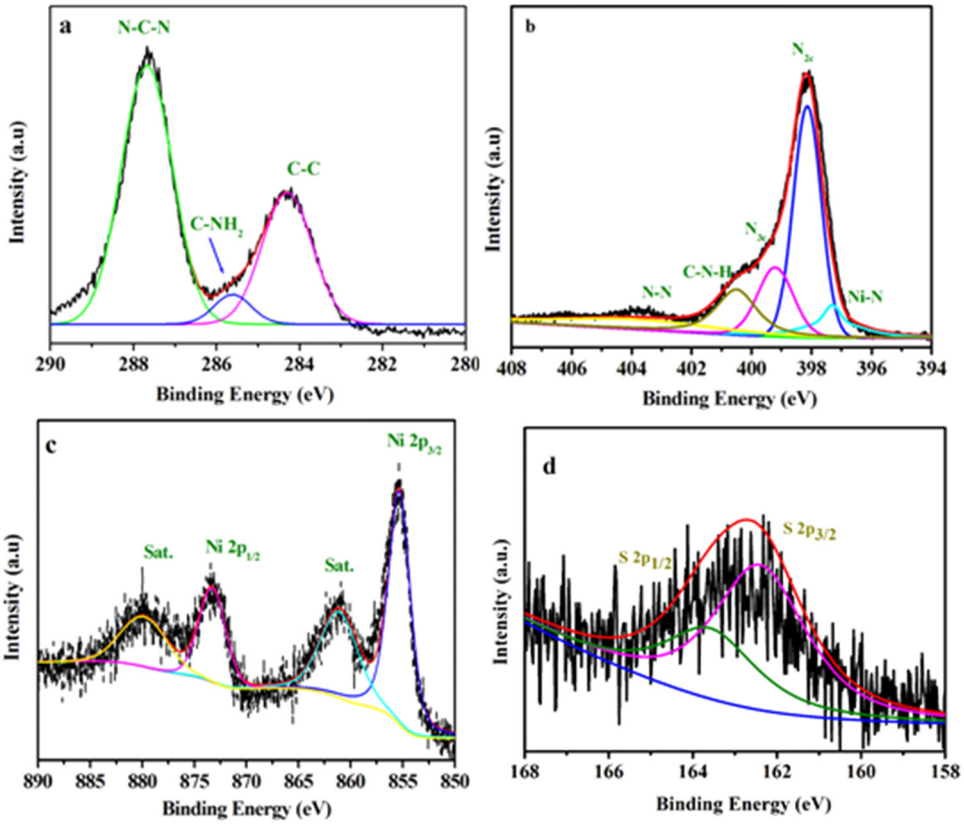

Fig. 3 High resolution XPS spectra of (a) C 1s, (b) N 1s, (c) Ni 2p, and (d) S 2p in Ni-ttc-d/g-C_3N_4.

H3 hysteresis loops, designating the mesoporous structure of the samples.[64] The specific surface area of 35-Ni-ttc-d/g-C_3N_4 was 4.335 m^2 g^{-1}, which is slightly lower than that of pure g-C_3N_4 (4.726 m^2 g^{-1}).

To specifically confirm the surface composition and electronic states, X-ray photoelectron spectroscopy (XPS) analysis was carried out for the samples. The XPS peaks were calibrated against the C1s peak at 284.6 eV. The survey scan of Ni-ttc and Ni-ttc-d displays Ni, S, and C (Fig. S5, ESI†). The Ni 2p spectrum of Ni-ttc and Ni-ttc-d (Fig. 2a and b) exhibits four peaks. Two peaks are observed around 871 and 853 eV, which are assigned to Ni $2p_{3/2}$ and $2p_{1/2}$ of Ni^{2+} states, respectively.[54,68] The other two peaks (879 eV and 861 eV) are the satellite peaks of Ni^{2+}. Two distinct peaks at 164 and 162 eV related to S $2p_{1/2}$ and S $2p_{3/2}$, respectively, are observed in the S 2p (Fig. 2c and d) spectra of Ni-ttc and Ni-ttc-d.

Fig. S6 (ESI†) indicates that 35-Ni-ttc-d/g-C_3N_4 consists of C, N, Ni, S, and O elements (Fig. S6, ESI†). Oxygen originates from the absorbed H_2O or CO_2 on the surface. The high-resolution C 1s XPS spectrum (Fig. 3a) demonstrates C–C and N–C–N bonding at 284.6, 285.9, and 288.0 eV, respectively.[68,69] The N 1s high-resolution spectrum (Fig. 3b) can be deconvoluted into five peaks at bonding energies of 397.3, 398.2, 399.2, 400.5, and 403.6 eV.[68,69] The strong peak at 398.2 eV is recognized as the sp^2-hybridized nitrogen, and the peak at 400.5 eV is observed due to the tertiary nitrogen N–$(C)_3$ groups. The low intensity peak that appeared at 397.3 eV is attributed to the metal

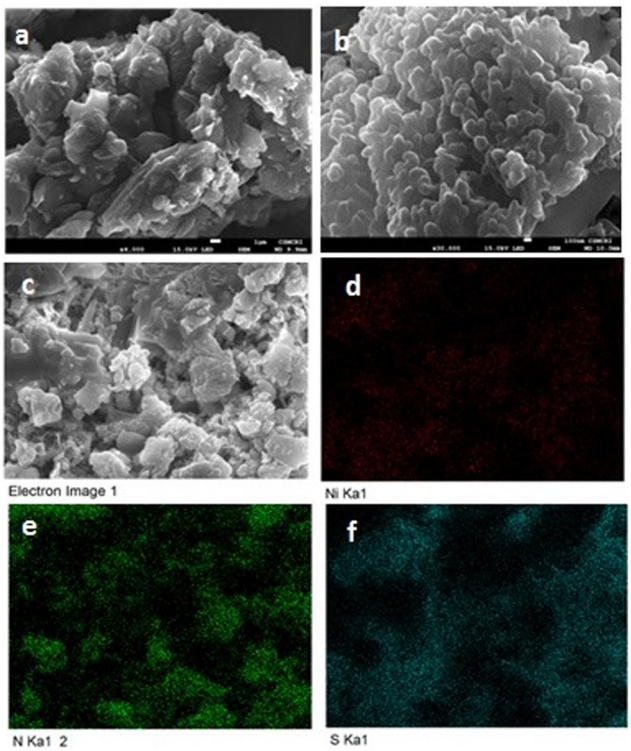

Fig. 4 (a and b) FESEM images of g-C_3N_4 and 35-Ni-ttc-d/g-C_3N_4, respectively, and (c–f) SEM-EDX elemental mapping of 35-Ni-ttc-d/g-C_3N_4.

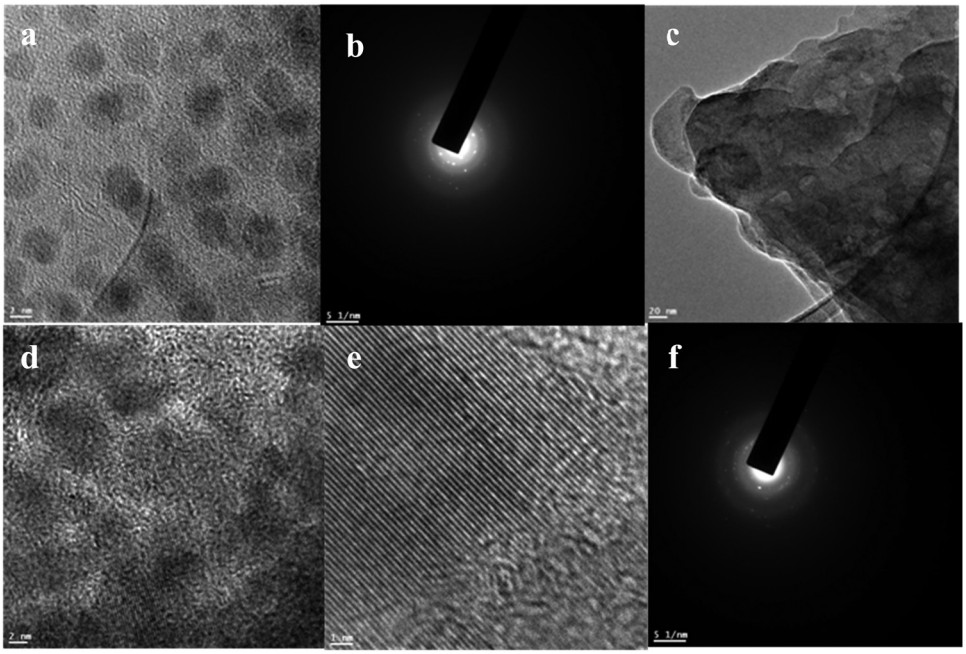

Fig. 5 (a and b) HRTEM and SAED images of Ni-ttc-d, (c and d) TEM images, (e) HRTEM, and (f) SAED pattern of 35-Ni-ttc-d/g-C_3N_4.

binding sp^2-hybridized nitrogen. The Ni 2p peaks of 35-Ni-ttc-d/g-C_3N_4, as illustrated in Fig. 3a, can be deconvoluted into two spin-orbit doublets and two shakeup satellites. The peaks near to 872 and 854 eV are assigned to the Ni $2p_{3/2}$ and $2p_{1/2}$ of Ni^{2+} states, respectively. The other two peaks (880 eV and 861 eV) are the satellite peaks of Ni^{2+}. The slightly higher binding energy for Ni^{2+} may be due to the binding with the sp^2-hybridized nitrogen of g-C_3N_4. The S demonstrated peaks (Fig. 3d) in the same binding energy range as obtained for Ni-ttc and Ni-ttc-d.

Fig. 4a and b display the FESEM images of g-C_3N_4 and 35-Ni-ttc-d/g-C_3N_4, respectively. The SEM-EDX particle mapping (Fig. 4c–f) indicates the presence of nickel, nitrogen and sulphur. The TEM image and SAED pattern of Ni-ttc-d are shown in Fig. 5a and b. The TEM image of Ni-ttc-d (Fig. 5a) indicates the presence of 3–4 nm spherical particles. The smooth, thin, and flat sheet-like morphology of g-C_3N_4 is visible in the TEM image of 35-Ni-ttc-d/g-C_3N_4 (Fig. 5c). The HR-TEM image (Fig. 5d) of the composite material confirms the presence of spherical Ni-ttc-d particles on the g-C_3N_4 surface. TEM-EDX mapping to show the homogeneous distribution of the elements is presented in Fig. S7 (ESI†).

Thermogravimetric analysis (TGA) was performed to study the stability of Ni-ttc and Ni-ttc-d, as depicted in Fig. 6. The TG plot for Ni-ttc illustrates three discrete weight losses up to 700 °C. Ni-ttc was found to be stable up to 180 °C, after which a steady and sharp mass loss of about 25% took place up to 270 °C. A further mass loss occurred gradually up to 700 °C. On the other hand, the Ni-ttc-d composite was thermally stable up to 275 °C, followed by an unsteady 20% weight loss between 275° and 700 °C, thus leaving a much higher quantity of residue than Ni-ttc at the same temperature. This demonstrates the superior thermal stability of Ni-ttc-d over Ni-ttc. The ICP-OES analysis shows 1.42% of nickel loading in the 35-Ni-ttc-d/g-C_3N_4 sample.

A series of electrochemical studies were then conducted to assess the electrocatalytic activity of the as-prepared catalysts *via* cyclic voltammetry (CV) in 1 M KOH and 1 M KOH with 0.33 M urea, using a typical three-electrode system. The concentration of urea in human urine is about 0.33 M and thus, the UOR was performed using this concentration. As shown in Fig. 7a, CV of 35-Ni-ttc-d/g-C_3N_4 was studied in KOH within the potential window of 0.65 to 1.65 *vs.* RHE with and without urea. It can be seen that in the absence of urea, the catalyst exhibited well defined redox peaks both in anodic and cathodic scans, which originated from the reversible transformation of Ni^{3+}/Ni^{2+}. The electrochemical active surface area (ECSA) was approximately

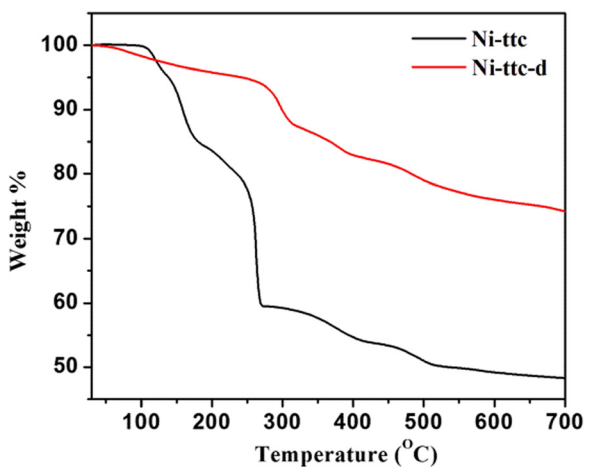

Fig. 6 TGA curves of Ni-ttc and Ni-ttc-d.

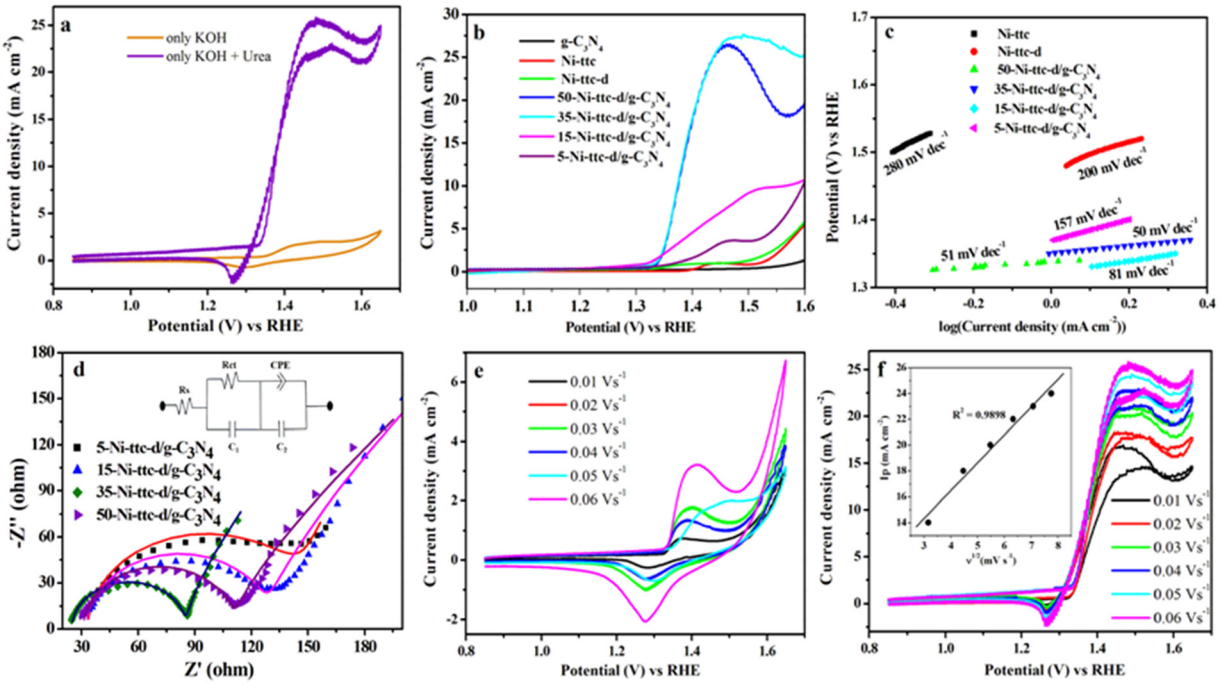

Fig. 7 (a) CV measurement of 35-Ni-ttc-d/g-C_3N_4 in N_2-saturated 1 M KOH solution in the absence and presence of 0.33 M urea (scan rate of 50 mV s^{-1}). (b) LSV recorded in N_2-saturated 1 M KOH solution and 0.33 M urea at 50 mV s^{-1} scan rate. (c) Tafel plots (scan rate of 5 mV s^{-1}), and (d) Nyquist plots of the different samples. CV measurement of 35-Ni-ttc-d/g-C_3N_4 at different scan rates (e) without urea, and (f) in 0.33 M urea solution.

estimated from the reduction peak, using the method (detail given in the ESI†) reported previously.[21,29]

$$\text{ECSA} = Q/0.257 \times m \quad (5)$$

The ECSA was calculated to be 0.6425, 1.36, 8.75, 27.25, 44.72, and 38.75 $m^2\ g^{-1}$ for Ni-ttc, Ni-ttc-d, 5-Ni-ttc-d/g-C_3N_4, 15-Ni-ttc-d/g-C_3N_4, 35-Ni-ttc-d/g-C_3N_4, and 50-Ni-ttc-d/g-C_3N_4, respectively (Table S2, ESI†). The gradual increase in the ECSA values indicates more active site availability. The CV measurement in the presence of 1 M KOH and 0.33 M urea portrayed a high oxidation current for 35-Ni-ttc-d/g-C_3N_4, which confirms the ability of the composite material for the UOR (Fig. 7a). The UOR activity of the different samples was then evaluated and is displayed in Fig. 7b and Fig. S8 (ESI†). The working oxidation potential corresponding to 10 mA cm^{-2} is a vital factor for estimating the UOR activity. The working oxidation potential at the current density of 10 mA cm^{-2} is found to be 1.38 V for both 35-Ni-ttc-d/g-C_3N_4 and 50-Ni-ttc-d/g-C_3N_4. Thus, a low overpotential of 150 mV is obtained at a current density of 10 mA cm^{-2}. The working oxidation potentials for 5-Ni-ttc-d/g-C_3N_4 and 15-Ni-ttc-d/g-C_3N_4 are significantly higher. The highest peak current density of 27.3 mA cm^{-2} is observed for 35-Ni-ttc-d/g-C_3N_4. The Tafel slope can be exploited to get more insight about the kinetics of the catalytic reaction. The Tafel plots for the different samples are presented in Fig. 7c. The smaller Tafel slope signifies lower resistance with increasing potential and faster UOR reaction rate. Both 35-Ni-ttc-d/g-C_3N_4 and 50-Ni-ttc-d/g-C_3N_4 exhibited comparable Tafel slopes of 50 and 51, respectively (Table S3, ESI†). Electrochemical impedance spectroscopy (EIS) studies were then carried out at 1.50 V (*vs.* RHE) to investigate in detail the electrical conductivity and ion transport kinetics (Fig. 7d and Fig. S9, ESI†). The charge-transfer resistance (R_{ct}) is found to be strongly related to the UOR, and the lowest R_{ct} of 60 Ω is observed for 35-Ni-ttc-d/g-C_3N_4 (Table S4, ESI†). Fig. 7e illustrates the CV measurement of the 35-Ni-ttc-d/g-C_3N_4 obtained in 1 M KOH with different scan rates from 10 to 60 mV s^{-1}. The current density of the oxidation and reduction peaks increases with the sweep rate enhancement, suggesting a diffusion-controlled reaction of OH^- ions at the electrode/electrolyte interface. Furthermore, the peak potentials are shifted towards the positive direction in the case of oxidation peaks and towards the negative direction for the reduction peaks; thus, the difference between the peak potentials gradually increased. A similar finding was obtained in the presence of 0.33 M urea and 1 M KOH as well, demonstrating increased current densities with the increasing scan rate (Fig. 7e). The double-layer capacitance (C_{dl}) and the corresponding ECSA were then evaluated and compared for Ni-ttc, Ni-ttc-d, and 35-Ni-ttc-d/g-C_3N_4 from the CV measurement recorded in the non-faradaic region at different scan rates and found to be 2.38, 2.82, and 6.74 mF cm^{-2}, respectively (Fig. S10 and Table S5, ESI†).

To assess the dependence of the efficiency of a catalyst on the concentration of the analyte, a series of CV measurements were performed in 1 M KOH solution containing different urea concentrations (0–1 M) and 0.33 M urea solution with different concentrations of KOH (0.1–2 M), as depicted in Fig. 8. It can be seen that the oxidation current improved as a function of urea concentration up to 0.5 M; however, the current increased at a reduced rate and then decreased slightly with the increase in concentration above 0.5 M, suggesting the saturation kinetics

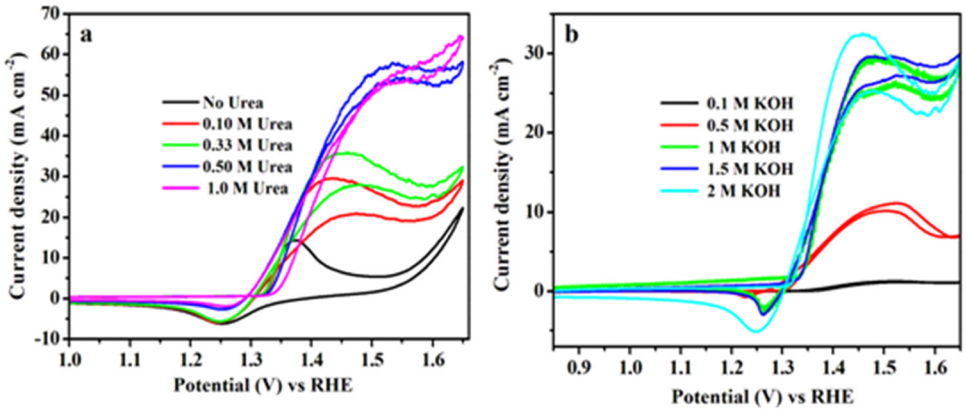

Fig. 8 CV responses of 35-Ni-ttc-d/g-C_3N_4 at a scan rate of 50 mV s^{-1} (a) with variable urea concentrations in fixed 1 M KOH solution saturated with N_2 and (b) with different KOH concentrations in fixed 0.33 M urea solution saturated with N_2.

of the urea reaction (Fig. 8a). Furthermore, at low KOH concentration, an insignificant increase in current was observed at fairly high overpotentials. At higher KOH concentrations, well resolved UOR peaks and Ni reduction peaks can be observed (Fig. 8b).

Stability is an additional key aspect for practical applications of the catalyst. To evaluate the long-term stability performance of 35-Ni-ttc-d/g-C_3N_4 for the UOR, an amperometric study at the electrode potential of 1.38 V *vs.* RHE has been conducted in the presence and absence of urea in the KOH solution. As presented in Fig. 9a, 35-Ni-ttc-d/g-C_3N_4 demonstrated excellent stability for 4 h (Fig. 9a). Furthermore, a potentiometric stability test of the catalyst was performed at a constant current density of 10 mA cm^{-2}. The catalyst showed excellent durability for over 30 h (Fig. 9b). It is worthwhile to mention that only a slight change in current density occurred after 100 cycles of catalytic scan (Fig. 9c and Fig. S11, ESI†). Fig. 9d shows the polarization curves for 35-Ni-ttc-d/g-C_3N_4 in the presence of urea (0.33 M) and without urea in the 1 M KOH solution.

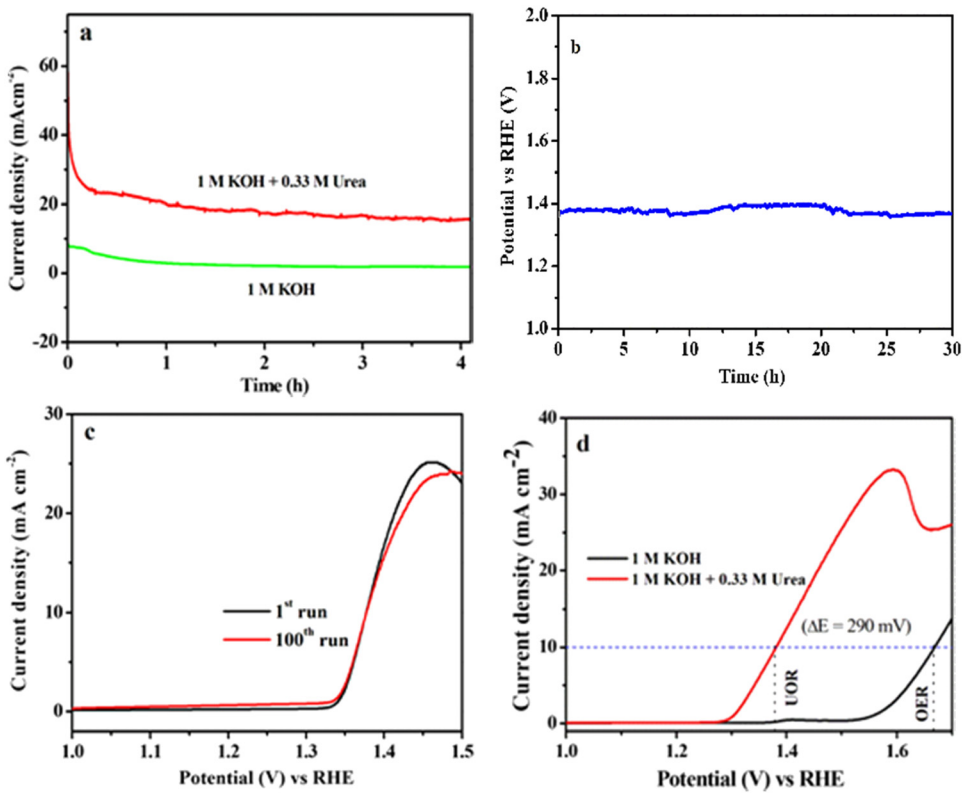

Fig. 9 (a) Chronoamperometric stability of 35-Ni-ttc-d/g-C_3N_4 in the absence and presence of 0.33 M urea in 1 M KOH. (b) Chronopotentiometric stability curve of 35-Ni-ttc-d/g-C_3N_4 in 0.33 M urea and 1 M KOH solution. (c) LSV curves of 35-Ni-ttc-d/g-C_3N_4 before and after the long-term UOR. (d) Polarization curves of 35-Ni-ttc-d/g-C_3N_4 with and without urea in the 1 M KOH solution.

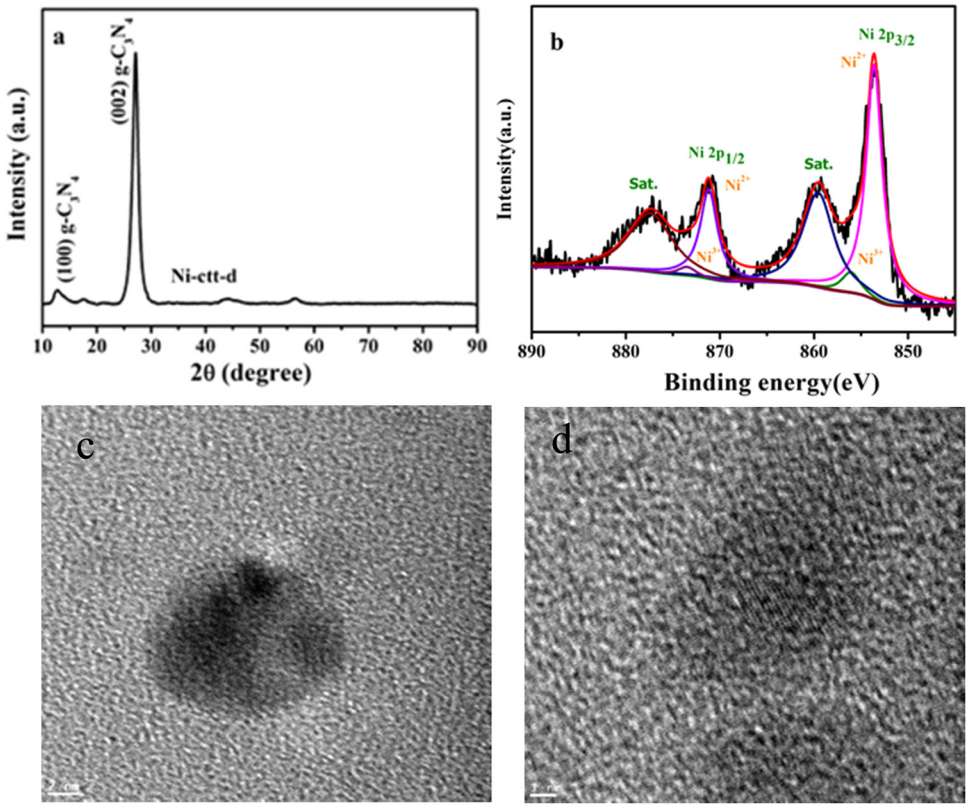

Fig. 10 (a) Powder XRD patterns of 35-Ni-ttc-d/g-C_3N_4 after the long-term UOR. (b) The Ni 2p XPS spectra of 35-Ni-ttc-d/g-C_3N_4 after the long-term UOR. (c and d) HRTEM images of 35-Ni-ttc-d/g-C_3N_4 after the long-term UOR.

The powder XRD patterns of 35-Ni-ttc-d/g-C_3N_4 remain the same before and after the stability test (Fig. 10a). The surface chemical states of the 35-Ni-ttc-d/g-C_3N_4 catalyst were then investigated using the XPS technique after the stability test. The formation of high valence Ni^{3+} species was observed in the XPS analysis (Fig. 10b). The morphology of the post catalytic sample of 35-Ni-ttc-d/g-C_3N_4 remains unaltered as evident from the HRTEM image (Fig. 10c and d).

Conclusions

In summary, an efficient nanocomposite catalyst for urea electro-oxidation is fabricated using a nano-structured nickel(II) trithiocarbonate complex and g-C_3N_4 *via* a mechanochemical method. The synthesis of nickel(II) trithiocarbonate is facile and simple, which makes fabrication reproducible and easy. The 35-Ni-ttc-d/g-C_3N_4 nanocomposite exhibits superior activity with a low overpotential of 150 mV at the working potential of 10 mA cm^{-2}, good kinetics, and durability towards the UOR. The nitrogenous functional groups present in g-C_3N_4 act as the perfect host to immobilize the nickel(II) complex. The impedance analysis indicates the improved charge transfer kinetics of 35-Ni-ttc-d/g-C_3N_4 for urea oxidation, reflected from the low charge-transfer resistance. The enhanced urea oxidation activity of 35-Ni-ttc-d/g-C_3N_4 is attributed to higher active site density and higher exchange current density. Therefore, with a high and stable current density as well as a low overpotential, 35-Ni-ttc-d/g-C_3N_4 is a capable anode catalyst for hydrogen generation *via* urea electrolysis, which opens a path for the development of low-cost and high-efficiency electrocatalysts for electrochemical hydrogen production based on other simple nickel(II) complexes. Moreover, the present work also explores the ability of g-C_3N_4, a recognized visible light photocatalyst, in electrocatalytic hydrogen generation.

Conflicts of interest

There are no conflicts to declare.

Acknowledgements

DG is thankful to IIEST Shibpur for providing fellowship. RB (IF 160999) and SNB (IF 170760) acknowledge the DST, India for providing an INSPIRE Fellowship. The authors acknowledge the SAIF, IIEST, Shibpur for providing NMR and HRMS facilities.

References

1 S. Peng, F. Gong, L. Li, D. Yu, D. Ji, T. Zhang, Z. Hu, Z. Zhang, S. Chou, Y. Du and S. Ramakrishna, *J. Am. Chem. Soc.*, 2018, **140**, 13644–13653.

2 M. Görlin, P. Chernev, J. F. de Araújo, T. Reier, S. Dresp, B. Paul, R. Krähnert, H. Dau and P. Strasser, *J. Am. Chem. Soc.*, 2016, **138**, 5603–5614.
3 X. Sun and R. Ding, *Catal. Sci. Technol.*, 2020, **10**, 1567–1581.
4 A. Nairan, P. Zou, C. Liang, J. Liu, D. Wu, P. Liu and C. Yang, *Adv. Funct. Mater.*, 2019, **29**, 1903747.
5 Z.-Y. Yu, C.-C. Lang, M.-R. Gao, Y. Chen, Q.-Q. Fu, Y. Duan and S.-H. Yu, *Energy Environ. Sci.*, 2018, **11**, 1890–1897.
6 S. Chen, J. Duan, A. Vasileff and S. Z. Qiao, *Angew. Chem., Int. Ed.*, 2016, **55**, 3804–3808.
7 Y. Zhao, S. Xing, X. Meng, J. Zeng, S. Yin, X. Lic and Y. Chen, *Nanoscale*, 2019, **11**, 9319–9326.
8 S. Chen, C. Wang, S. Liu, M. Huang, J. Lu, P. Xu, H. Tong, L. Hu and Q. Chen, *J. Phys. Chem. Lett.*, 2021, **12**, 4849–4856.
9 M. Zhang, Z. Wang, Z. Duan, S. Wang, Y. Xu, X. Li, L. Wang and H. Wang, *J. Mater. Chem. A*, 2021, **9**, 18323–18328.
10 H. Xu, K. Ye, K. Zhu, J. Yin, J. Yan, G. Wang and D. Cao, *Inorg. Chem. Front.*, 2020, **7**, 2602–2610.
11 M. Li, X. Deng, K. Xiang, Y. Liang, B. Zhao, J. Hao, J.-L. Luo and X.-Z. Fu, *ChemSusChem*, 2020, **13**, 914–924.
12 H.-Y. Sun, G.-R. Xu, F.-M. Li, Q.-L. Hong, P.-J. Jin, P. Chen and Y. Chen, *J. Energy Chem.*, 2020, **47**, 234–240.
13 D. R. McCubbin, B. J. Apelberg, S. Roe and F. Divita, *Environ. Sci. Technol.*, 2002, **36**, 1141–1146.
14 L. Wang, Z. Liu, S. Zhu, M. Shao, B. Yang and J. G. Chen, *ACS Appl. Mater. Interfaces*, 2018, **10**, 41338–41343.
15 H. Yang, M. Yuan, Z. Sun, D. Wang, L. Lin, H. Li and G. Sun, *ACS Sustainable Chem. Eng.*, 2020, **8**, 8348–8355.
16 J. Meng, P. Chernev, M. R. Mohammadi, K. Klingan, S. Loos, C. Pasquini, P. Kubella, S. Jiang, X. Yang, Z. Cui, S. Zhu, Z. Li, Y. Liang and H. Dau, *Electrochim. Acta*, 2019, **318**, 32–41.
17 J. Xie, L. Gao, S. Cao, W. Liu, F. Lei, P. Hao, X. Xia and B. Tang, *J. Mater. Chem. A*, 2019, **7**, 13577–13584.
18 R. G. Jadhav and A. K. Das, *Nanoscale*, 2020, **12**, 23596–23606.
19 D. Wang, W. Yan, S. Vijapur and G. Botte, *J. Power Sources*, 2012, **217**, 498–502.
20 W. Yan, D. Wang, L. D. Aldana and G. Botte, *Electrochim. Acta*, 2014, **134**, 266–271.
21 R. K. Singh and A. Schechter, *Electrochim. Acta*, 2018, **278**, 405–411.
22 W. Simka, J. Piotrowski, A. Robak and G. Nawrat, *J. Appl. Electrochem.*, 2009, **39**, 1137–1143.
23 W. Simka, J. Piotrowski and G. Nawrat, *Electrochim. Acta*, 2007, **52**, 5696–5703.
24 W. Zhu, Z. Yue, W. Zhang, N. Hu, Z. Luo, M. Ren, Z. Xu, Z. Wei, Y. Suo and J. Wang, *J. Mater. Chem. A*, 2018, **6**, 4346–4353.
25 B. K. Boggs, R. L. King and G. G. Botte, *Chem. Commun.*, 2009, 4859–4861.
26 W. Yang, X. Yang, B. Li, J. Lin, H. Gao, C. Hou and X. Luo, *J. Mater. Chem. A*, 2019, **7**, 26364.
27 R. L. King and G. G. Botte, *J. Power Sources*, 2011, **196**, 9579–9584.
28 L. Sha, J. Yin, K. Ye, G. Wang, K. Zhu, K. Cheng, J. Yan, G. Wang and D. Cao, *J. Mater. Chem. A*, 2019, **7**, 9078.
29 R. P. Forslund, J. T. Mefford, W. G. Hardin, C. T. Alexander, K. P. Johnston and K. J. Stevenson, *ACS Catal.*, 2016, **6**, 5044–5051.
30 J. Xie, W. Liu, F. Lei, X. Zhang, H. Qu, L. Gao, P. Hao, B. Tang and Y. Xie, *Chem. – Eur. J.*, 2018, **24**, 18408–18412.
31 V. Vedharathinam and G. G. Botte, *Electrochim. Acta*, 2013, **108**, 660–665.
32 S. Periyasamy, P. Subramanian, E. Levi, D. Aurbach, A. Gedanken and A. Schechter, *ACS Appl. Mater. Interfaces*, 2016, **8**, 12176–12185.
33 W. Yan, D. Wang and G. Botte, *Electrochim. Acta*, 2012, **61**, 25–30.
34 Z. Yue, S. Yao, Y. Li, W. Zhu, W. Zhang, R. Wang, J. Wang, L. Huang, D. Zhao and J. Wang, *Electrochim. Acta*, 2018, **268**, 211–217.
35 L. Wang, M. Li, Z. Huang, Y. Li, S. Qi, C. Yi and B. Yang, *J. Power Sources*, 2014, **264**, 282–289.
36 D. Wang, W. Yan, S. H. Vijapur and G. G. Botte, *Electrochim. Acta*, 2013, **89**, 732–736.
37 H. Liu, Z. Liu and L. Feng, *Nanoscale*, 2019, **11**, 16017–16025.
38 S. Hu, S. Wang, C. Feng, H. Wu, J. Zhang and H. Mei, *ACS Sustainable Chem. Eng.*, 2020, **8**, 7414–7422.
39 H. Yang, M. Yuan, Z. Sun, D. Wang, L. Lin, H. Li and G. Sun, *ACS Sustainable Chem. Eng.*, 2020, **8**, 8348–8355.
40 J. Ge, Y. Lai, M. Guan, Y. Xiao, J. Kuang and C. Yang, *Environ. Sci.: Nano*, 2021, **8**, 1326–1335.
41 T.-H. Wu and B.-W. Hou, *Catal. Sci. Technol.*, 2021, **11**, 4294–4300.
42 M. Yuan, R. Wang, Z. Sun, L. Lin, H. Yang, H. Li, C. Nan, G. Sun and S. Ma, *Inorg. Chem.*, 2019, **58**, 11449–11457.
43 Y. Xu, X. Chai, T. Ren, S. Yu, H. Yu, Z. Wang, X. Li, L. Wang and H. Wang, *Chem. Commun.*, 2020, **56**, 2151–2154.
44 S. Wang, X. Yang, Z. Liu, D. Yanga and L. Feng, *Nanoscale*, 2020, **12**, 10827–10833.
45 H. Xu, K. Ye, K. Zhu, Y. Gao, J. Yin, J. Yan, G. Wang and D. Cao, *Inorg. Chem. Front.*, 2021, **8**, 2788–2797.
46 R. L. King and G. G. Botte, *J. Power Sources*, 2011, **196**, 2773–2778.
47 V. Vedharathinam and G. G. Botte, *Electrochim. Acta*, 2012, **81**, 292–300.
48 D. A. Daramola, D. Singh and G. G. Botte, *J. Phys. Chem. A*, 2010, **114**, 11513–11521.
49 W. Xu, Z. Wu and S. Tao, *Energy Technol.*, 2016, **4**, 1329–1337.
50 K. Ye, D. Zhang, F. Guo, K. Cheng, G. Wang and D. Cao, *J. Power Sources*, 2015, **283**, 408–415.
51 R. M. A. Hameed and S. S. Medany, *J. Colloid Interface Sci.*, 2018, **513**, 536–548.
52 B. Yang, D. Bin, T. Tian, Y. Liu and B. Liu, *ChemElectroChem*, 2017, **5**, 659–664.
53 L. Wang, T. Du, J. Cheng, X. Xie, B. Yang and M. Li, *J. Power Sources*, 2015, **280**, 550–554.
54 R. Banerjee, D. Ghosh, Kirti, D. K. Chanda, A. Mondal, D. N. Srivastava and P. Biswas, *Electrochim. Acta*, 2022, **408**, 139920.

55 B. Pieber, J. A. Malik, C. Cavedon, S. Gisbertz, A. Savateev, D. Cruz, T. Heil, G. Zhang and P. H. Seeberger, *Angew. Chem., Int. Ed.*, 2019, **58**, 9575–9580.
56 C. Cavedon, A. Madani, P. H. Seeberger and B. Pieber, *Org. Lett.*, 2019, **21**, 5331–5334.
57 X. Wang, K. Maeda, A. Thomas, K. Takanabe, G. Xin, J. M. Carlsson, K. Domen and M. Antonietti, *Nat. Mater.*, 2009, **8**, 76–80.
58 A. Savateev, I. Ghosh, B. König and M. Antonietti, *Angew. Chem., Int. Ed.*, 2018, **57**, 15936–15947.
59 A. Vijeta and E. Reisner, *Chem. Commun.*, 2019, **55**, 14007–14010.
60 I. Ghosh, J. Khamrai, A. Savateev, N. Shlapakov, M. Antonietti and B. König, *Science*, 2019, **365**, 360–366.
61 J. Liu, Y. Liu, N. Liu, Y. Han, X. Zhang, H. Huang, Y. Lifshitz, S.-T. Lee, J. Zhong and Z. Kang, *Science*, 2015, **347**, 970–974.
62 W.-J. Ong, L.-L. Tan, Y. H. Ng, S.-T. Yong and S.-P. Chai, *Chem. Rev.*, 2016, **116**, 7159–7329.
63 A. Vijeta, C. Casadevall, S. Roy and E. Reisner, *Angew. Chem., Int. Ed.*, 2021, **60**, 8494–8499.
64 S. Martha, A. Nashim and K. M. Parida, *J. Mater. Chem. A*, 2013, **1**, 7816–7824.
65 Y. Lin, K. A. Watson, M. J. Fallbach, S. Ghose, J. G. Smith, Jr., D. M. Delozier, W. Cao, R. E. Crooks and J. W. Connell, *ACS Nano*, 2009, **3**, 871–884.
66 A. P. Amrute, J. De Bellis, M. Felderhoff and F. Scheth, *Chem. – Eur. J.*, 2021, **27**, 6819–6847.
67 J. Feng, D. Zhang, H. Zhou, M. Pi, X. Wang and S. Chen, *ACS Sustainable Chem. Eng.*, 2018, **6**, 6342–6349.
68 H. Liu, Q. He, H. Jiang, Y. Lin, Y. Zhang, M. Habib, S. Chen and L. Song, *ACS Nano*, 2017, **11**, 11574–11583.
69 X. Yue, S. Yi, R. Wang, Z. Zhang and S. Qiu, *Sci. Rep.*, 2016, **6**, 22268.